(2)

Computational Modeling of Three-Dimensional Compressible Leading Edge Vortices

by

Earll M. Murman

Final Report
ONR Grant N00014-86-C-0288

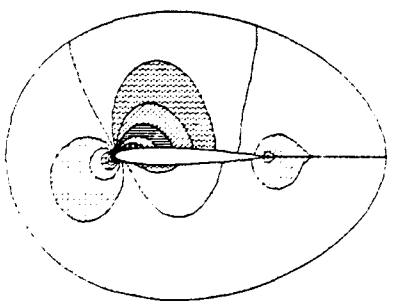

COMPUTATIONAL FLUID DYNAMICS LABORATORY

Department of Aeronautics and Astronautics

Massachusetts Institute of Technology
Cambridge, Massachusetts 02139

(2)

Computational Modeling of Three-Dimensional Compressible Leading Edge Vortices

by

Earll M. Murman

Final Report
ONR Grant N00014-86-C-0288

Final Report
ONR Contract N00014-86-C-0288
MIT OSP No. 97568

Computational Modeling of Three-Dimensional Compressible Leading Edge Vortices

Reporting Period
February 15, 1986 - January 31, 1990

Submitted to

Dr. Spiro Lekoudis
Mechanics Divsion
Office of Naval Research
800 N. Quincy Street
Arlington, VA 22217-5000
(202) 696-4404

Submitted by
Professor Earll M. Murman
Principal Investigator
Department of Aeronautics and Astronautics
Massachusetts Institute of Technology
Cambridge, MA 02139

Submitted April 10, 1989

1 Summary

The research supported under this grant focussed on the accurate computation of compressible leading-edge vortex flows with interpretation and understanding of the results. To this end, a number of investigations were undertaken, starting with the conical Euler equation model and concluding with fully three-dimensional Navier-Stokes equation calculations. Considerable emphasis was placed on :

- Comparisons of Euler with Navier-Stokes calculations to understand the origins of various mechanisms;
- Comparison of calculations with experiments both to determine the accuracy of the calculations and to comprehend the physical processes; and
- Interpretation of the results with the aid of analytical models.

A summary of some of the work is contained in the paper by Murman, Goodsell , and Malecki [1] presented at Symposium Transsonicum III which is attached as Appendix I. The major contributions are contained in the thesis of the participating students, namely:

- Doctoral Students
  1. Kennth Grant Powell, Vortical-Solutions of the Conical Euler Equations [2]
  2. Bernard Loyd, A Semi-Implicit Navier-Stokes Solver and its application to a Study of Separated Flow about Blunt Delta Wings [3]
- Masters Students
  1. Robert E. Malecki, Euler-Equation Calculations for a Cropped-Delta Wing Using the CYBER 205 [4]
  2. Aga Myung Goodsell, 3-D Euler Calculations of Vortex Flows Over Delta Wings [5]
  3. Jorge Pérez-Sánchez, Numerical Simulation of Deceleration of an Axisymmetric Vortex [6].

Other papers and articles resulting from the research are cited in the following sections and listed in the References section.

2 Conical Euler Solutions

The conical Euler equation model was adopted to provide a computationally tractable approach for understanding the essential features of vortical flow represented by inviscid mechanisms. Conical calculations are valid for steady supersonic freestream Mach numbers and bodies which have conical self-similarity. The wings must have a sharp leading edge so that the Kutta condition yields a realistic model for the separation point.

The PhD thesis of Powell [2] contains a thorough description of the numerical method, numerous computed results, comparisons with experiments, and interpretation of the findings. Calculations were done for delta wings at various angles of attack and yaw, and for delta wings with leading edge flaps. It was found that to achieve adequate mesh resolution in the region of the leading edge vortex, local refinement was needed. An embedded mesh strategy was developed and applied to most of these cases. This is reported in the paper by Powell and Murman [7]. Figures 1-4 on the following pages present representative results from this study. These are for a flat plate delta wing with a 75° leading edge sweep at 12° angle of attack, 8° of yaw and a freestream Mach number of 1.7.

A parallel investigation [8] involved a comparsion of the conical Euler equaton results with experiments and conical Navier-Stokes equation calculations. The cases were all for supersonic freestream Mach numbers, but included three leading edge sweep angles and five angles of attack. Although the Euler equation solutions predicted the major flow regimes quite well, the Navier-Stokes solutions were in somewhat better agreement with the data as might be expected. This paper was selected as the best Applied Aerodynamics Paper in 1987 by the AIAA.

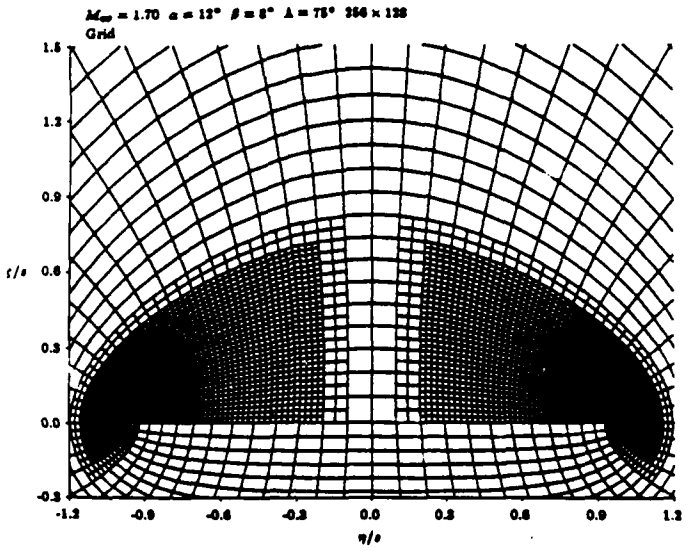

Figure 1 - Grid showing two levels of embedding

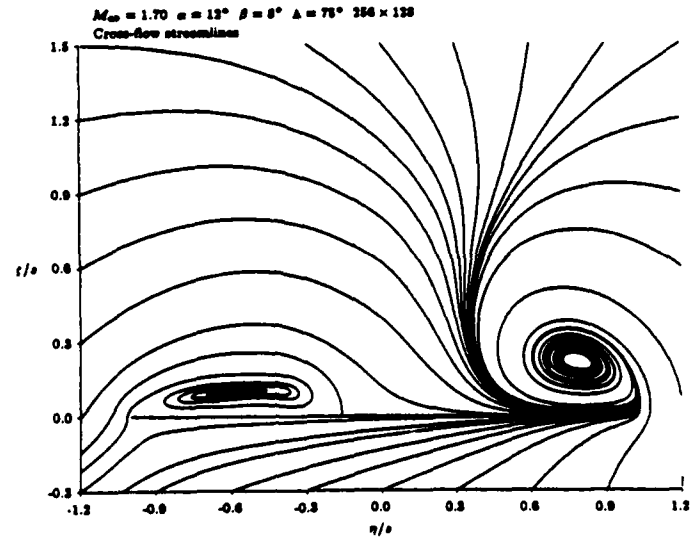

Figure 2 - Cross-flow streamlines showing topology of the vortices

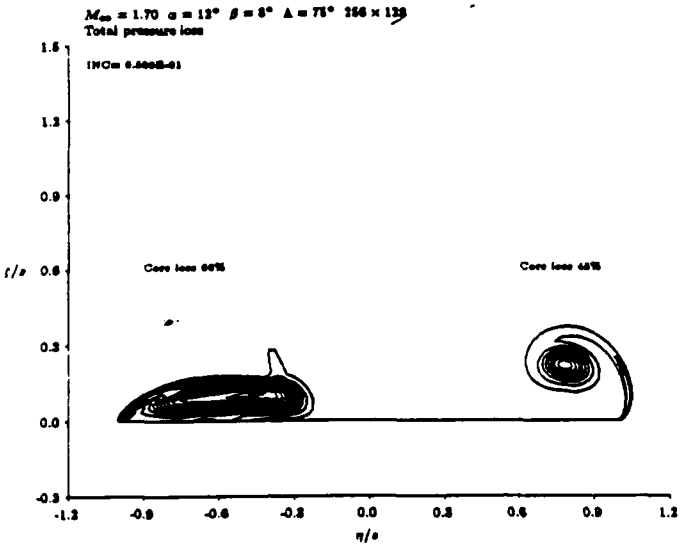

Figure 3 - Total pressure loss

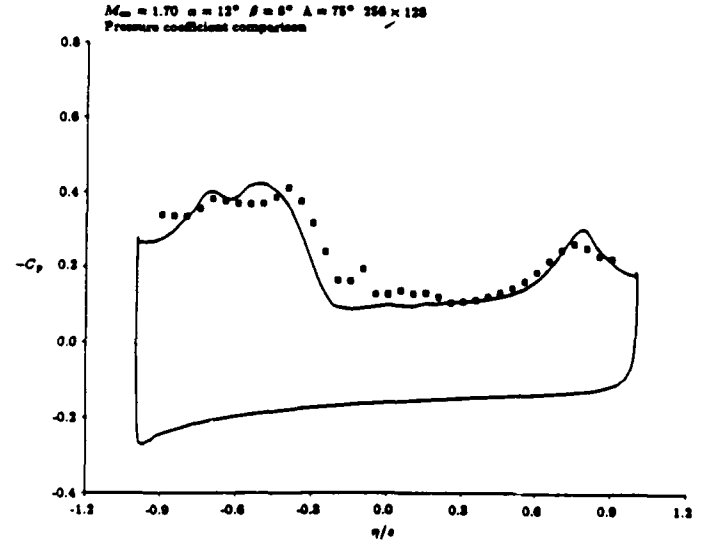

Figure 4 - Comparison of surface pressure coefficient with data

3 Total Pressure Loss

A question of considerable interest is what is the origin of the large total pressure losses in the cores of the vortices, as indicated in Figure 3. The Euler equations alone do not contain any dissipative mechanism. However, in their discrete form, both added and implicit artifical viscosity are present and necessary. A paper was written by Murman, et al [9] which discussed this issue. The paper contained an error in the cross-flow streamline integration scheme which led to some wrong conclusions that were later corrected [10].

The work of Powell [2] conclusively showed that the total pressure losses are by and large independent of both second and fourth difference damping coefficients, ϵ_2 and ϵ_4 respecitvely, as well as grid refinement. The tables on the following page present these results. Figures 5 and 6 and the tables indicate that the overall vortex dimensions (width and height) are less sensitive to these parameters than is the region of large total pressure loss (core size).

Powell proceeded to formulate a theoretical model for the core of a viscous vortex by deriving a self-similarity theory for an incompressible, conical vortex [2,11]. The model predicted that the total pressure loss is determined by the magnitude of the swirl velocity at the edge of the vortex, and not by the magnitude of the viscosity. The total pressure loss is related to the dissipation mechanism, and apparently the numerical viscosity is a reasonable representation of physical viscosity for some cases. Powell also showed that the Reynolds number based upon artifical viscosity is so large in the region of the vortex that it would dominate real visous terms in most Navier-Stokes calculations. This is discussed further in Appendix I.

Finally, based upon the observation that the total pressure loss in the vortex might be related to bursting, a preliminary study was done to look at the effects of decelerating an axisymmetric inviscid rotational flow [6].

ϵ_2	ϵ_4	Loss Level	Core Size	Vortex Width	Vortex Height
0.003	0.0010	37.4%	1.00	1.00	1.00
0.003	0.0003	37.6%	0.32	1.10	1.13
0.003	0.0030	38.2%	1.74	1.08	1.02
0.001	0.0010	37.2%	0.71	0.97	1.01
0.010	0.0010	37.6%	1.67	1.11	1.08

Table 1: Effects of artificial viscosity level on loss

Equivalent grid	Loss Level	Core Size	Vortex Width	Vortex Height
64 × 64	33.9%	2.55	1.39	1.43
128 × 128	37.6%	1.00	1.00	1.00
256 × 256	35.1%	0.26	0.96	1.05

Table 2: Effects of grid refinement on loss

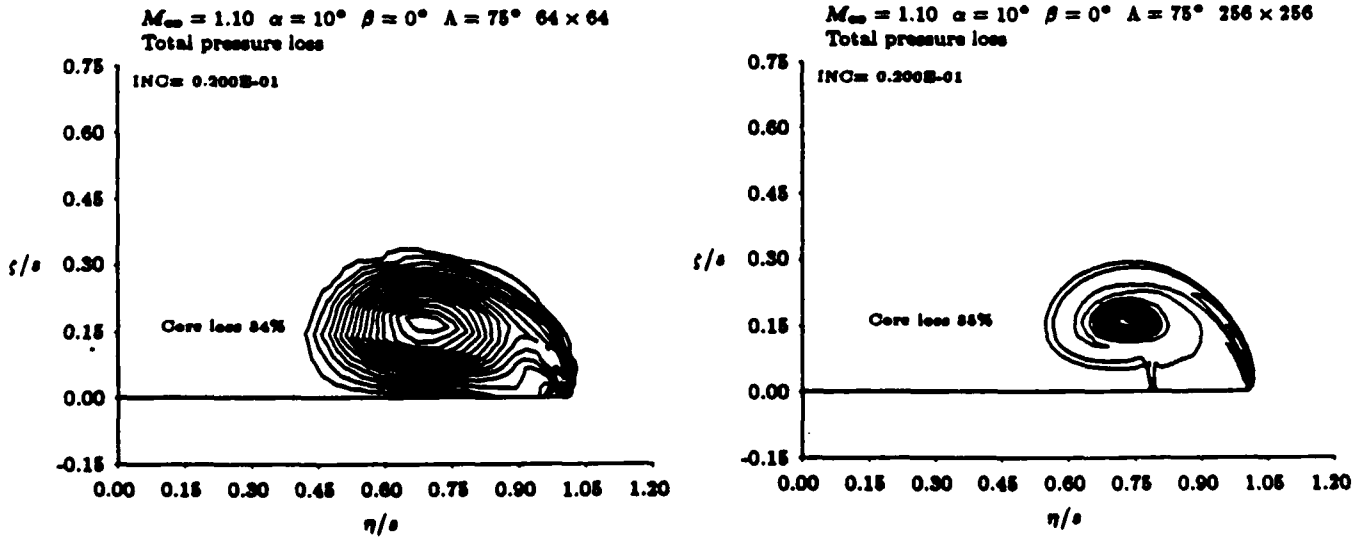

Figures 5 and 6 - Total pressure losses; 64 × 64 & 256 × 256 grids.

4 Three-Dimensional Euler Equations

Three studies were undertaken [4,5,12] based upon three-dimensional Euler equation calculations. In the first study, Malecki [4] vectorized an existing Euler solver for the CYBER 205 and used an O-O grid supplied by Rizzi to compute the flow about a cropped delta wing model tested in the Netherlands. The study showed that significant levels of artificial viscosity were needed to obtain an converged solution, apparently due to high grid skewness.

Goodsell [5] revamped the solver to perform on an O-H grid and proceeded to compute not only the same transonic cases that Malecki had done, but also supersonic and subsonic cases. Representative results of both of these studies are contained in the paper of Appendix I [1].

The third study done by Lee and Murman [12] utilized Goodsell's Euler solver for a preliminary study of the effects of the vortex from a closely coupled canard on the following wing. Representative results are given in Figures 7 and 8.

The three-dimensional Euler calculations showed that the absence of secondary separation which is not included in the Euler model had substantial effects on the predicted pressure distributions in the transonic regime, necessitating the development of a Navier-Stokes model. Supersonic cases are much less sensitive to this effect [8].

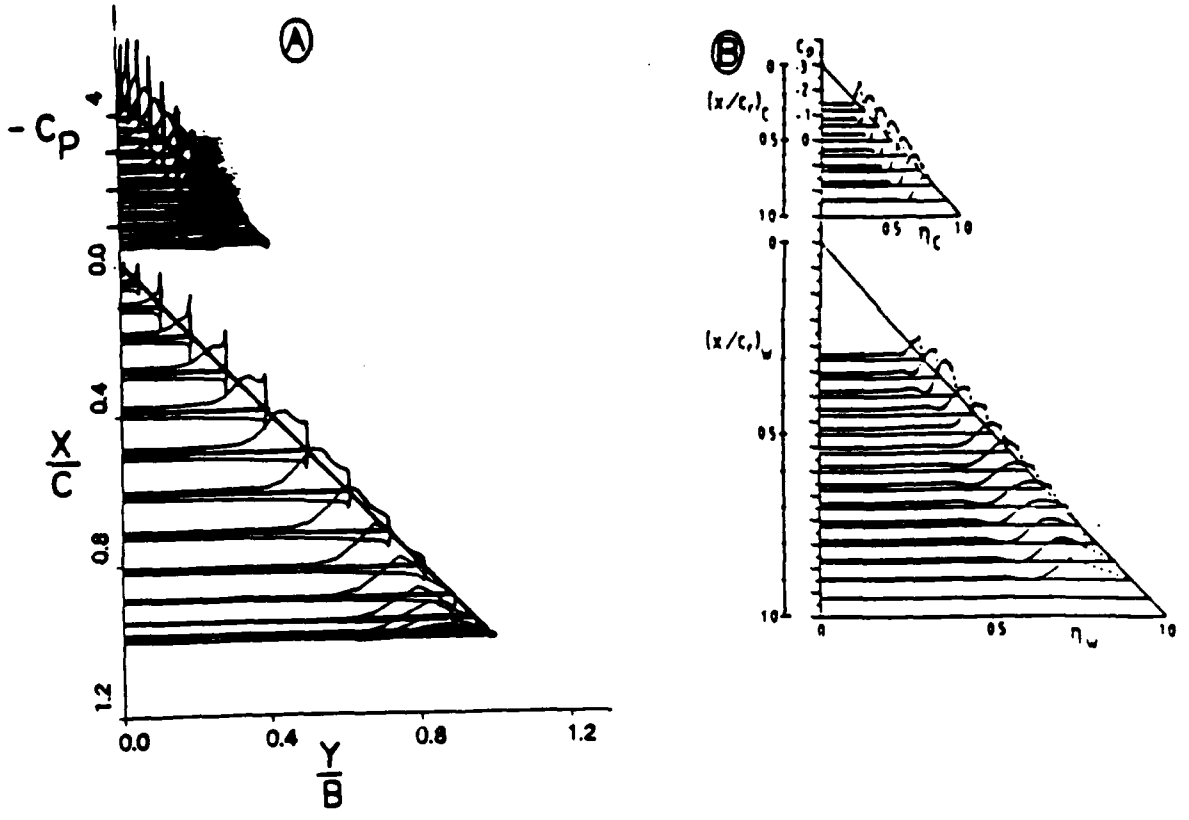

Figure 7: Canard-on pressure surface distribution
a. Computational b. Experimental
$\alpha = 8.8°$

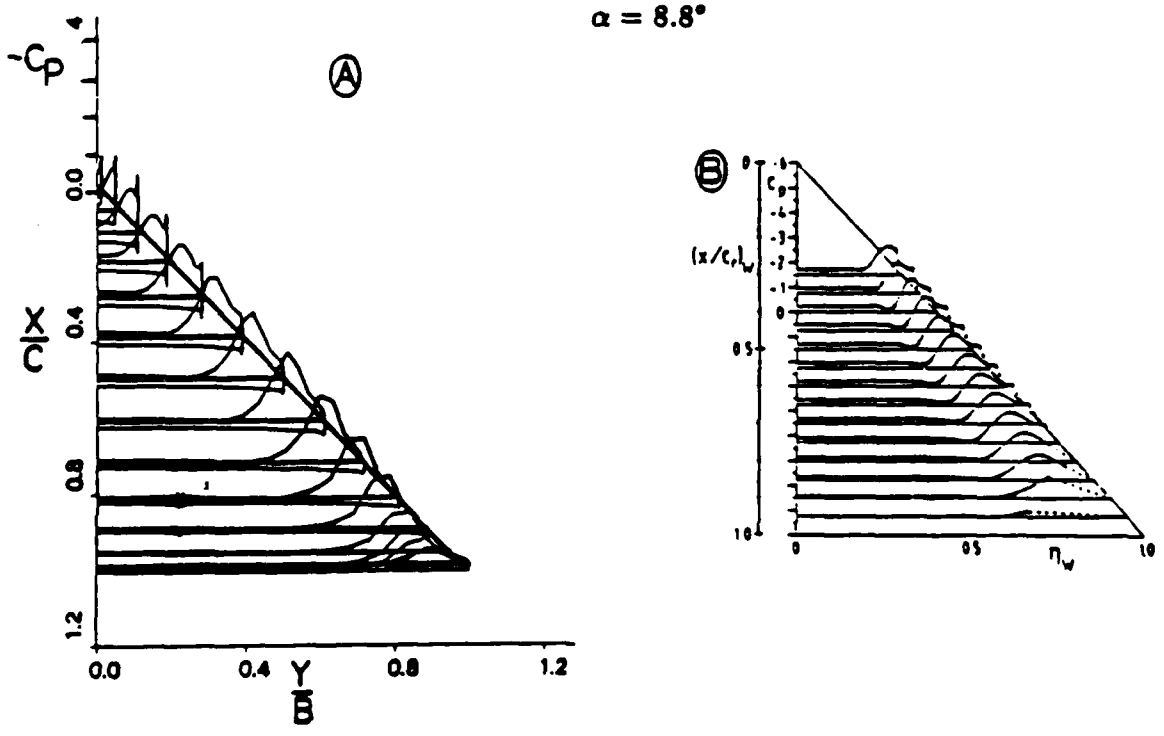

Figure 8: Canard-off surface pressure distribution
a. Computational. b. Experimental
$\alpha = 8.8°$

5 Three-Dimensional Navier-Stokes Solutions

Two studies were done for three-dimensional Navier-Stokes equations. The first was undertaken by Rizzi who spent a summer at MIT as part of this project. In this regard, he modified his existing Euler solver to add the full Navier-Stokes terms, and then proceeded to compare the Euler and Navier-Stokes results [13] for a round leading edge version of the cropped delta wing studied by Malecki and Goodsell. Representative results shown in Figure 9 indicate that the viscous calculations are in much better agreement with experiments than are the inviscid ones.

The second study was undertaken by Loyd [3,14] who added the thin layer Navier-Stokes terms to Goodsell's code and used a newly developed semi-implicit method to solve them. Loyd particularly focussed on the mechanisms of leading edge separation for laminar flows over a family of swept conical delta wings. Detailed analysis indicated both shock-free and shock-induced separation at the leading edge. The other features of primary and secondary vortical flows were also observed. A representative result from this study is shown in Figure 10.

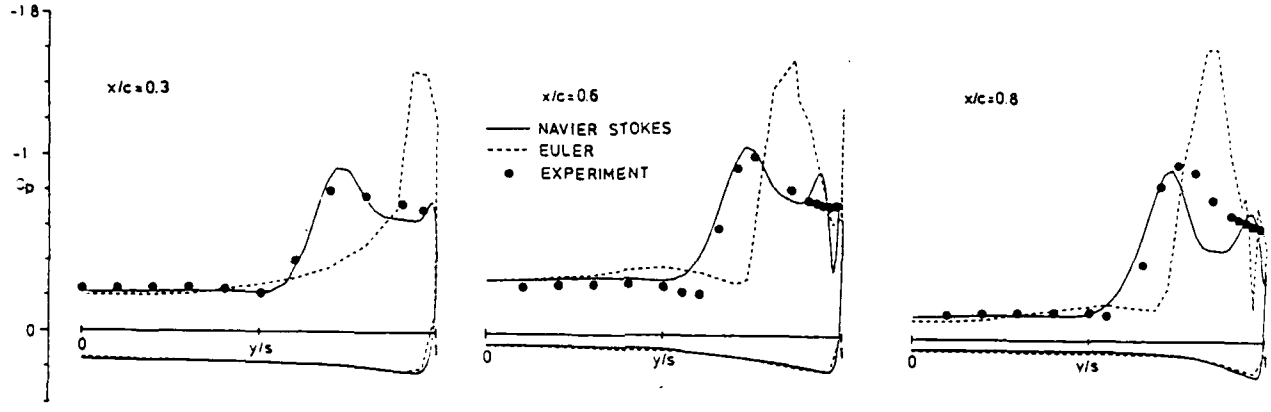

Figure 9 - Measured and computed C_p distributions [13]

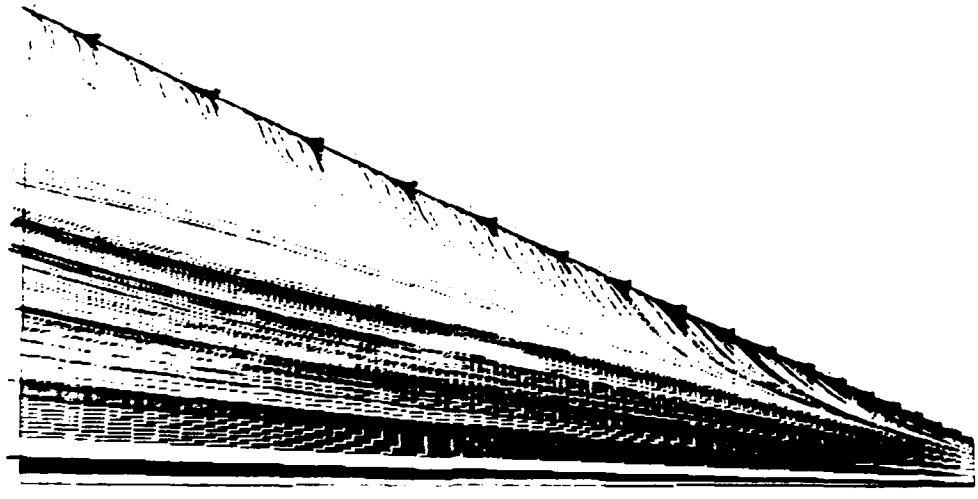

Figure 10 - Numerical oil flow picture, $M_\infty = 1.6$, $\alpha = 4°$

References

[1] E.M. Murman, A.M. Goodsell, and R.E. Malecki. Transonic Vortical Flow. In J. Zierep and H. Oertel, editors, *Symposium Transsonicum III*, pages 265–279, IUTAM, Springer-Verlag, May 1988.

[2] Kenneth Grant Powell. *Vortical Solutions of the Conical Euler Equations.* PhD thesis, Massachusetts Institute of Technology, June 1987. To be published by Vieweg as a Volume of Notes On Numerical Fluid Mechanics. Also MIT CFDL TR-87-8.

[3] Bernard Loyd. *A Semi-Implicit Navier-Stokes Solver and its Application to a Study of Separated Flow about Blunt Delta Wings.* PhD thesis, Massachusetts Institute of Technology, February 1989. Also MIT CFDL TR-89-2.

[4] Robert Edward Malecki. *Euler Equation Calculations for a Cropped Delta Wing Using the CYBER 205.* Master's thesis, Massachusetts Institute of Technology, August 1986. Also MIT CFDL TR-86-4.

[5] Goodsell Aga Myung. *3-D Euler Calculations of Vortex Flows Over Delta Wings.* Master's thesis, Massachusetts Institute of Technology, July 1987. Also MIT CFDL TR-87-6.

[6] Jorge M. Pérez-Sánchez. *Numerical Simulation of Deceleration of an Axisymmetric Vortex.* Master's thesis, Massachusetts Institute of Technology, May 1989. Also MIT CFDL TR-89-1.

[7] K.G. Powell and E.M. Murman. An Embedded Mesh Procedure for Leading-Edge Vortex Flows. In *Transonic Symposium: Theory, Application, and Experiment*, pages 231–259, NASA CP 3020, April 1988.

[8] S.N. McMIllin, J.L. Thomas, and E.M. Murman. Euler and Navier-Stckes Solutions for the Leeside Flow Over Delta Wings at Supersonic Speeds. *AIAA J. of Aircraft*, 26(5):452–459, May 1989. Also AIAA-87-2270.

[9] E.M. Murman, K.G. Powell, A. M. Goodsell, and M. Landahl. *Leading Edge Vortex Solutions With Large Total Pressure Losses.* AIAA 87-0039, January 1987.

[10] E.M. Murman and K.G. Powell. Trajectory Integration in Vortical Flows. *AIAA J.*, 27(7):982–984, July 1989.

[11] K.G. Powell and E.M. Murman. *A Model for the Core of a Slender Viscous Vortex.* AIAA 88-0503, January 1988.

[12] K.M. Lee and E.M. Murman. *A Comparison of Experimental and Preliminary Numerical Results for Close Coupled Canard-Wing.* MIT CFDL-TR-88-8, May 1988.

[13] A. Rizzi, B. Müller, and C. Purcell. Comparison of Euler and Navier-Stokes Solutions for Vortex Flow Over a Delta-Wing. In *AIAA 5th Applied Aerodynamics Conference*, pages 154–163, August 1987. AIAA 87-2347.

[14] B. Loyd, K. Lee, and E. Murman. *Semi-Implicit Navier-Stokes Solver (SINSS) Calculations of Separated Flows Around Blunt Delta Wings.* AIAA 90-0590, January 1990.

TRANSSONIC VORTICAL FLOW

by

Earll M. Murman
Aga M. Goodsell
Robert E. Malecki

CDFL-TR-88-10 May 1988

Paper presented at Transsonicum Symposium III, Göttingen, Germany, May 24-28, 1988. To appear in Symposium Proceedings published by Springer-Verlag

Transsonic Vortical Flow

EARLL M. MURMAN, AGA M. GOODSELL[1], ROBERT E. MALECKI[2]

Computational Fluid Dynamics Laboratory
Department of Aeronautics and Astronautics
Massachusetts Institute of Technology
Cambridge, MA 02139

Introduction

Transonic flow is generally associated with the inviscid fluid effects when a flow with a freestream Mach number $M_\infty \simeq 1$ accelerates to locally supersonic velocities, or decelerates to locally subsonic velocities, as it moves streamwise past a body. However, transonic flows can occur in many other circumstances such as on high lift devices at low M_∞, at the tips of helicopter blades, and around corners in ducts. In this paper, a class of transonic flows for slender, highly swept wings at high angle of attack ($\alpha \geq 10°$) will be considered. Under these conditions, leading edge vortices generally form as shown schematically in Figure 1. If $M_\infty \sim 1$, the streamwise flow can be transonic in the classical sense, leading to mixed subsonic-supersonic flow and shock waves on the wing. However, the leading edge vortices create additional transonic cross flow effects due to the high swirl velocities associated with them.

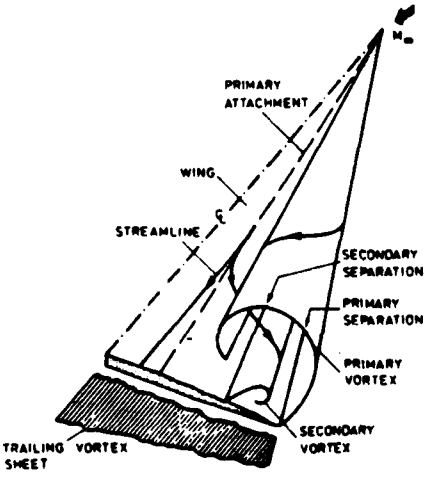

Figure 1: Schematic Flow Field

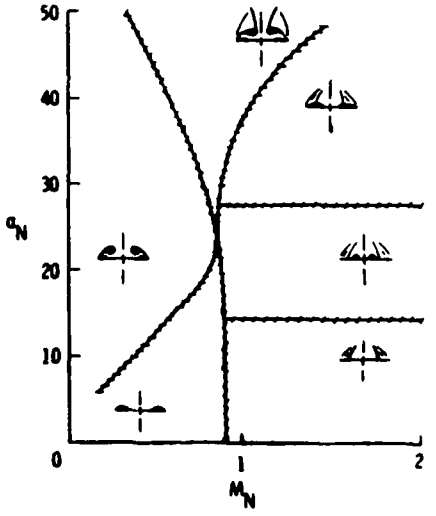

Figure 2: Classification of Flow Regimes

The classes of vortical transonic crossflows are generally correlated in terms of the angle of attack and Mach number normal to the wing leading edge given by the formulas [1]

$$\alpha_n = \tan^{-1}(\tan\alpha \sec\Lambda) \tag{1}$$

$$M_n = M_\infty \sin\alpha \csc\alpha_n \tag{2}$$

where Λ is the wing leading edge sweep angle. Figure 2 shows a correlation from experimental data presented and discussed by Miller and Wood [2,3] for sharp leading edge wings. Other flow

[1]Present address, NASA Ames Research Center, Moffett Field, CA.
[2]Present Address, Pratt & Whitney Aircraft Group, Hartford, Conn.

patterns have also been discovered experimentally by Vorropoulos and Wendt [4] and Szodruch and Peake [5]. A paper in this conference by Narayan and Seshadri [6] further discusses these flow regimes and also presents results for round leading edge wings. For the latter case, a Reynolds number based on some leading edge length scale must also be an important parameter.

Transonic vortical flows are a complex mixture of streamwise and crossflow effects. The paper by Elsenaar and Bütefisch [7] presents results of an extensive experimental investigation for a 65° delta wing which serve to illustrate this point. A complete model which can handle the interacting inviscid and viscous effects undoubtedly requires Navier-Stokes equations, and one such approach is given by Rizzi, Drougge, and Müller [8]. For sharp leading edge wings, the separation of the flow to form a primary vortex is fixed by the geometry via a Kutta condition, and an Euler equation model should be adequate if vorticity is introduced. However, important viscous effects such as shock wave boundary layer interaction, secondary vortex formation, and boundary layer transition clearly won't be represented. Although the question of whether such models can represent vortex breakdown is not settled, numerical solutions seem to indicate that bursting of the primary vortex is captured if the mesh is fine enough. In principle, a potential flow with added vortex sheets or filaments as suggested by Desai et al [9] could be used. However, the direct solution of the Euler and/or Navier-Stokes equations seems more promising, although more expensive.

In this paper, Euler equation models are considered for sharp edge geometries. The conical Euler equations are considered first to investigate the crossflow phenomena. Following this is a discussion of the origin of the vorticity in Euler equation calculations. To conclude the paper, three-dimensional solutions are presented which combine both streamwise and crossflow transonic effects. The geometry considered is that reported by Elsenaar and Bütefisch [7].

Governing Equations

The three-dimensional unsteady Euler equations in conservation form are:

$$\frac{\partial}{\partial t}\begin{bmatrix}\rho\\ \rho u\\ \rho v\\ \rho w\\ \rho E\end{bmatrix}+\frac{\partial}{\partial x}\begin{bmatrix}\rho u\\ \rho u^2+p\\ \rho uv\\ \rho uw\\ u\left(\rho E+p\right)\end{bmatrix}+\frac{\partial}{\partial y}\begin{bmatrix}\rho v\\ \rho uv\\ \rho v^2+p\\ \rho vw\\ v\left(\rho E+p\right)\end{bmatrix}+\frac{\partial}{\partial z}\begin{bmatrix}\rho w\\ \rho uw\\ \rho vw\\ \rho w^2+p\\ w\left(\rho E+p\right)\end{bmatrix}=0. \tag{3}$$

$(u,v,w)=\vec{u}$ are the Cartesian velocity components in the x,y,z directions, respectively, ρ is the density, E the total energy per unit mass, and p the static pressure given by the equation of state

$$\frac{p}{\rho}=(\gamma-1)\left[E-\frac{u^2+v^2+w^2}{2}\right]. \tag{4}$$

Unsteady terms have been retained for the iterative procedure used to reach the steady solution. The tangential flow boundary condition is enforced on the solid body while the Kutta condition will be enforced implicitly by the numerical method. Freestream conditions are applied far away from the body.

Introducing the conical variables

$$\eta=\frac{y}{x}\qquad \xi=\frac{z}{x}\qquad r=\sqrt{x^2+y^2+z^2} \tag{5}$$

and assuming conical self-similarity (the solution is independent of r), the Euler equations

become

$$\frac{r}{\sqrt{1+\eta^2+\xi^2}}\frac{\partial}{\partial t}\begin{bmatrix}\rho\\ \rho u\\ \rho v\\ \rho w\\ \rho E\end{bmatrix}+\frac{\partial}{\partial \eta}\begin{bmatrix}(v-\eta u)\rho\\ (v-\eta u)\rho u-\eta p\\ (v-\eta u)\rho v+p\\ (v-\eta u)\rho w\\ (v-\eta u)(\rho E+p)\end{bmatrix}+\frac{\partial}{\partial \xi}\begin{bmatrix}(w-\xi u)\rho\\ (w-\xi u)\rho u-\xi p\\ (w-\xi u)\rho v\\ (w-\xi u)\rho w+p\\ (w-\xi u)(\rho E+p)\end{bmatrix}+2\begin{bmatrix}\rho u\\ \rho u^2+p\\ \rho uv\\ \rho uw\\ u(\rho E+p)\end{bmatrix}=0. \tag{6}$$

These equations are valid for wing geometries generated by rays passing through the origin and for $M_\infty > 1$ so that the outer boundary condition is also conical. Again, the unsteady terms are retained only for the iterative solution process. The equations are solved on the unit sphere by setting r = 1. Boundary conditions are the same as the Euler equations except that freestream conditions are applied ahead of the conical bow shock.

Solution Procedure

The basic solution scheme is a finite volume spatial discretization with a multi-stage integration in time, as proposed by Jameson *et al* [10]. It will be outlined for the conical Euler equations. The solution of the three-dimensional Euler equations, which is very similar, is fully explained by Roberts [11] who implemented the version used in this paper.

The conical Euler equations (6) written in vector form

$$\frac{\partial}{\partial t}\mathbf{U}+\frac{\partial}{\partial \eta}\mathbf{F}+\frac{\partial}{\partial \xi}\mathbf{G}+\mathbf{H}=0 \tag{7}$$

may be transformed using the divergence theorem into an integral equation and discretized as

$$\frac{d\mathbf{U}_{ij}}{dt}A_{ij}+\sum_{\ell=1}^{4}\left[\mathbf{F}_\ell n_{\xi_\ell}+\mathbf{G}_\ell n_{\eta_\ell}\right]+\mathbf{H}_{ij}A_{ij}=0. \tag{8}$$

A_{ij} is the area of a computational cell and the summation represents the fluxes through the four cell sides with normal vectors $\vec{n}_\ell = (n_{\xi_\ell}, n_{\eta_\ell})$. The flux vectors $\mathbf{F}_\ell, \mathbf{G}_\ell$ on the cell sides are evaluated from simple averages of flux vectors at the cell centers $\mathbf{F}_{ij}, \mathbf{G}_{ij}$ and $\mathbf{F}_{i\pm1,j\pm1}, \mathbf{G}_{i\pm1,j\pm1}$. A multistage integration scheme is used to solve the equations in time to reach a steady state. In order to accelerate the iterative solution, the time step in each cell is determined by the linear stability criteria for that cell. Since the time steps are different for each cell, the solution is not time accurate. The tangential flow boundary condition on the body is enforced by zeroing the convective fluxes in (6) and extrapolating the pressure from the adjacent cell center, $p_{j_{body}} = p_{j_{i=1}}$.

This scheme requires added second and fourth order damping to capture shocks and damp unwanted high frequency modes of the discrete solutions. The damping formulation follows Rizzi and Eriksson [12]. The second order damping is pressure-weighted, and is of the form

$$\mathbf{D}_2(\mathbf{U})=\nu_2\left[\delta_i\left(\frac{\delta_i^2 p}{max|\delta_i^2 p|}\delta_i\mathbf{U}\right)+\delta_j\left(\frac{\delta_j^2 p}{max|\delta_j^2 p|}\delta_j\mathbf{U}\right)\right] \tag{9}$$

where δ_i and δ_j are undivided central difference operators defined by

$$\delta_i(\mathbf{U}_{i,j})=\mathbf{U}_{i+\frac{1}{2},j}-\mathbf{U}_{i-\frac{1}{2},j} \qquad \delta_j(\mathbf{U}_{i,j})=\mathbf{U}_{i,j+\frac{1}{2}}-\mathbf{U}_{i,j-\frac{1}{2}}. \tag{10}$$

The fourth-order damping is unweighted, and of the form

$$\mathbf{D}_4(\mathbf{U})=\nu_4\left[\delta_i^4\mathbf{U}+\delta_j^4\mathbf{U}\right]. \tag{11}$$

The pressure switch in the second order damping is normalized to vary from $O(\Delta^2)$ to 1 throughout the flow field, where Δ is a measure of the mesh spacing. It is designed to turn on at embedded shock waves. In these calculations it was found that the second difference damping needed to be turned on at the wing leading edge. This was done by setting the pressure switch to 1 in a few cells in this region. Values of $\nu_2 = .05$ and $\nu_4 = .01$ were used for the calculations unless noted.

The added damping terms (9) and (11) together with the basic discretization error from (8) implies that the numerical calculations represent the solution of a modified differential equation

$$\frac{\partial}{\partial \eta}\mathbf{F} + \frac{\partial}{\partial \xi}\mathbf{G} + \mathbf{H} \simeq \nu_2 \tilde{\lambda}\Delta\left[\frac{\partial}{\partial \xi}\left(S_\xi \frac{\partial \mathbf{U}}{\partial \xi}\right) + \frac{\partial}{\partial \eta}\left(S_\eta \frac{\partial \mathbf{U}}{\partial \eta}\right)\right] + O\left(\Delta^2\right) - \nu_4 \tilde{\lambda}\Delta^3\left[\frac{\partial^4 \mathbf{U}}{\partial \xi^4} + \frac{\partial^4 \mathbf{U}}{\partial \eta^4}\right] \tag{12}$$

where S_ξ, S_η are the pressure switches in (9) and $\tilde{\lambda}$ the maximum characteristic speed of propagation of a disturbance $\simeq |\vec{u}| + c$. The first group of terms on the right hand side represents the second order damping, the second group the truncation errors, and the third group the fourth order damping. In the neighborhood of the tip and embedded shock waves, $S_\xi, S_\eta \sim 1$ and the second difference damping is proportional to the first power of the mesh spacing. Away from these regions, $S_\xi, S_\eta \sim \Delta^2$ and the second difference damping is proportional to the cube of the mesh spacing. The fourth difference damping is everywhere proportional to the cube of the mesh spacing. The solutions automatically satisfy the Kutta condition, and the present authors believe this is due to the added numerical viscosity.

Conical Euler Solutions

Numerous solutions have been computed for the conical Euler equations for sharp edge geometries using the method as outlined above or in a somewhat modified form. All the primary vortex and shock wave structures illustrated in Figure 2 have been reproduced, as well as other shock structures reported in [4,5]. Secondary vortices due to boundary layer separation under the primary vortex and vortices created by shock wave-boundary layer interactions are not modeled by the Euler equations. The most comprehensive presentation of the variety of solutions which have been obtained may be found in the PhD thesis of Powell [13]. A comparison of the conical and a three-dimensional Euler solution are given in [14], while comparisons between the conical Euler and conical Navier-Stokes solutions with data are given in [15]. In this section, two representative examples will be presented.

An interesting example illustrating the nature of the transonic crossflow effects is a flat plate delta wing with a leading edge sweep $\Lambda = 75°$ in a $M_\infty = 1.95$ flow at an angle of attack $\alpha = 25°$. The above conditions correspond to $M_n = .94, \alpha_n = 61°$ and fall in the middle top region of Figure 2. Experimental results for this condition are reported by Monnerie and Werlé [16]. The calculations were done on an O-type grid which had 128 cells around the wing, windward to leeward symmetry plane, and 128 cells between the wing and the farfield boundary outside the bow shock.

The general topology of the flow field is illustrated in Figure 3 by the conical streamlines which are everywhere tangential to the crossflow velocity vectors. The view corresponds to looking upstream from the trailing edge with only the right hand side of the wing shown. The dominant feature is the sheet emanating from the wing leading edge and spiraling into the vortex core[3]. On the windward side, the attachment line is almost halfway between the centerline and leading edge of the wing, while on the leeward side it is at the wing centerline.

[3]The blank area in the middle of the core is due to an inaccurate streamline integration [17] and not an apparent source as suggested in [18].

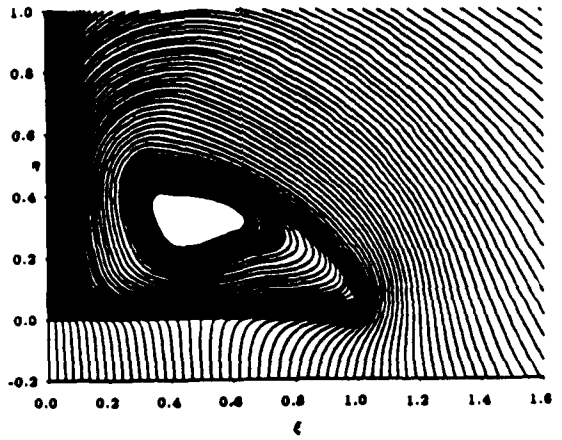

Figure 3: Conical streamlines.

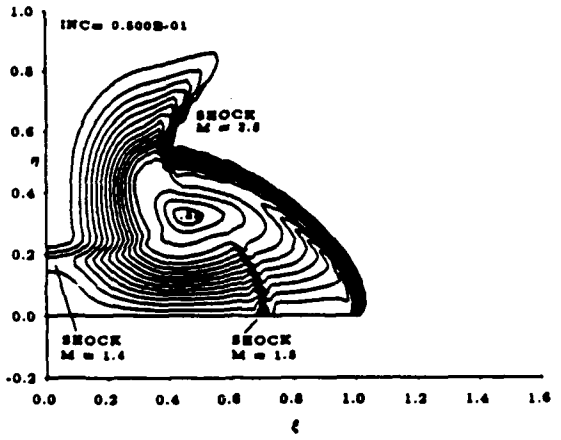

Figure 4: Total Pressure Loss.

Contours of constant total pressure loss $1-(P_t/P_{t_\infty})$ are shown in Figure 4. There are large losses in the shear layer from the leading edge, and in the center of the vortex the total pressure loss is 88 %. It can be seen that cross flow shocks are present above and below the primary vortex and that there is also a shock between the two primary vortices. This latter shock is observed in the shadowgraph picture from the experiment [16]. The swirling flow accelerates to cross flow Mach number $M_c = 2.5$ above the vortex before passing through the first shock. It then turns downwards towards the wing reaching $M_c = 1.4$ ahead of a second shock. The flow then accelerates to $M_c = 1.8$ on the wing surface under the vortex where it experiences the third shock. A comparison of the cross flow streamlines and the shock locations will reveal a sort of transonic nozzle effect for the last two shocks. There is a minimum spacing between the vortex and the symmetry plane and the vortex and the wing. Examination of the crossflow Mach number contours which aren't shown here reveals a converging-diverging nozzlelike pattern.

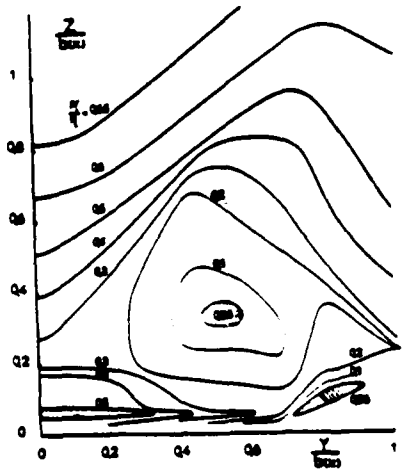

Figure 5: Experimental pitot pressure.

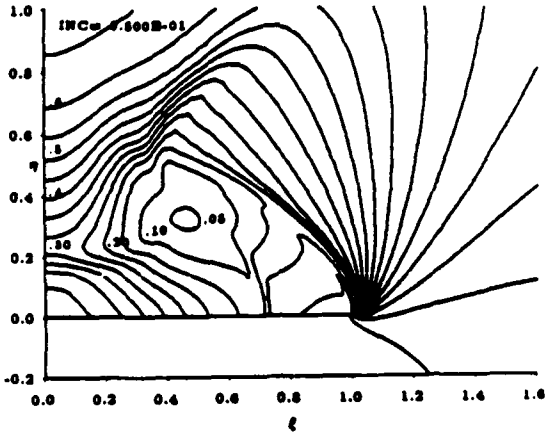

Figure 6: Computed pitot pressures.

Monnerie and Werlé reported measured pitot pressure (normalized by the freestream total pressure) values on the leeside of the wing which are shown in Figure 5. Pitot pressures computed from the Euler calculations using the Rayleigh pitot formula [19] are shown in Figure 6. The computed values would correspond to a probe which is everywhere aligned with the flow, while in the experiments the probe was aligned with the wing centerline. Vortical flows have large flow angularity as illustrated by the swirl angle (ratio of cross flow velocity magnitude to

radial velocity) contours of Figure 7. Generally, pitot pressure measurements are accurate to within 1% if the flow angularity is less than 10° [20]. This is really only true right in the vortex core region, and the computed (.05) and measured (.06) values are in excellent agreement. Throughout the rest of the region there is good qualitative agreement except where the wing boundary layer and secondary vortex formation dominate.

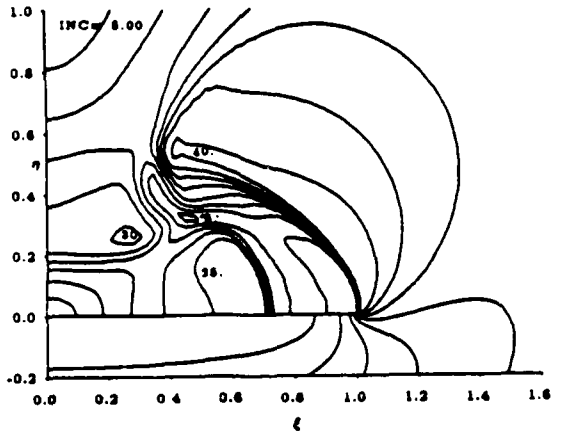

Figure 7: Computed swirl angles.

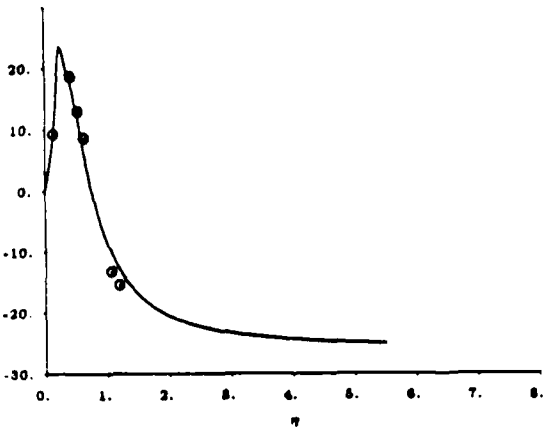

Figure 8: Symmetry plane flow angles.

Measurements were also made of the flow angle in the leeside symmetry plane. A small wedge in the flow was adjusted until the top and bottom shock waves viewed with a shadowgraph were symmetric. The estimated accuracy[4] is ±2°. Figure 8 compares the measured and computed values which are in good agreement. The change in flow angularity across the shock spanning the port and starboard vortices is clear.

Calculations have been done on coarser grids to investigate the sensitivity of the solution to grid resolution. The following table displays some of these values.

Grid	32 × 32	64 × 64	128 × 128
η vortex	.287	.307	.320
ξ vortex	.445	.470	.438
Normal Force Coefficient	.729	.739	.742
Max Swirl Angle	38°	40°	40°
Max Total Pressure loss	.872	.882	.880
Min Pitot Pressure	.075	.052	.048

It can be seen that the position of the vortex, the normal force coefficient, the maximum total pressure loss, and maximum swirl angle are all insensitive to mesh spacing. The pitot pressure is somewhat sensitive to grid refinement as the streamwise Mach number in the vortex core increases with finer meshes. This is consistent with the computed vortex core size becoming smaller with mesh refinement. In general, the solution on the 128 × 128 grid can be considered converged except for the size and details of the inner vortex core region[13]. However, its position and maximum total pressure loss are converged as illustrated in the table. The conclusions are representative of all our conical Euler calculations for supersonic freestream flows.

The second example of a conical Euler solution is taken from [15] which presents six different comparisons between conical Euler, conical Navier-Stokes, and experimental results. Details of the calculations and comparisons may be found in that paper. The particular example presented here is for a delta wing with a leading edge sweep $\Lambda = 75°$ in a $M_\infty = 2.8$ flow at an angle of

[4]Personal communication between authors.

attack $\alpha = 8°$. These parameters give $M_n = .82, \alpha_n = 28.5°$ which lie in the left middle region of Figure 2.

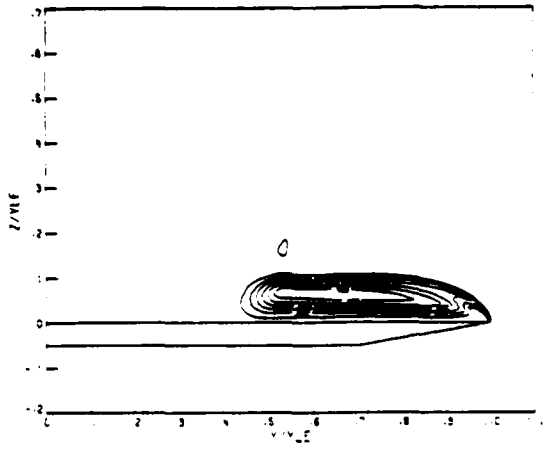

Figure 9: Total pressure loss, Euler.

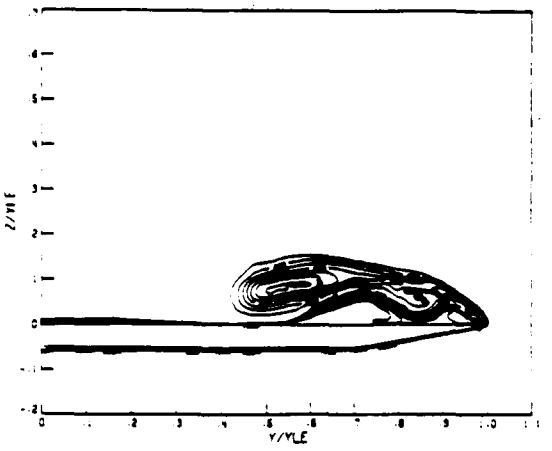

Figure 10: Total pressure loss, Navier-Stokes.

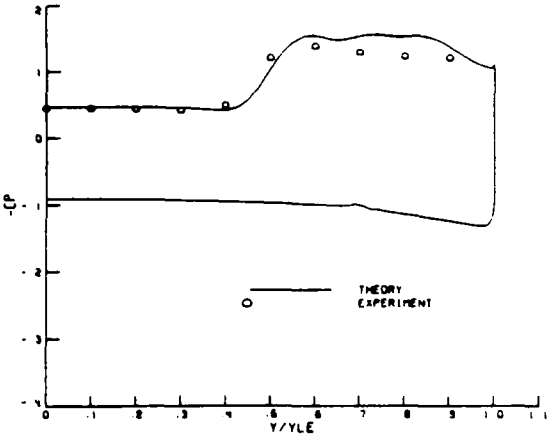

Figure 11: C_p, Euler and data.

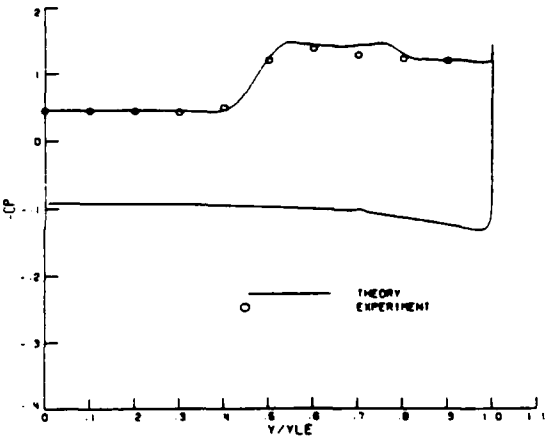

Figure 12: C_p, Navier-Stokes and data.

A comparison of the total pressure loss contours between the conical Euler and conical Navier-Stokes (laminar) is given by Figures 9 and 10. The Navier-Stokes model clearly shows the viscous boundary layer, the secondary separation, and for this case a tertiary separation. The latter affect the position and shape of the primary vortex by their displacement effects. However, both the Euler and Navier-Stokes models yield a primary vortex with essentially the same total pressure loss in the core. A comparison of the surface pressures given in Figures 11 and 12 shows that both models are in reasonable agreement with the data. The effects of the secondary and tertiary vortex (including their displacement effects on the primary vortex) are small, but well represented by the Navier-Stokes solution.

Total Pressure Loss

The origin of the total pressure loss in the Euler equation solutions is not immediately apparent and has been the source of considerable controversy. The total pressure loss can

equivalently be represented as entropy (S) production, and by Crocco's equation

$$T\nabla S + \vec{u} \times \vec{\omega} = \nabla h_o \tag{13}$$

can be related to a vorticity ($\vec{\omega}$) distribution since the total enthalpy (h_o) is constant for this class of flows. One source of total pressure loss is the conical bow shock wave. However, these losses are two to three orders of magnitude smaller than the values in the vortical regions. The results shown in Figures 3 to 8 contain strong embedded shocks which clearly have an associated total pressure loss. Comparing Figures 3 and 4 it can be seen that these losses are approximately convected along streamlines. There are additional total pressure losses in the shear layer from the wing tip and vortex core. The latter is clearly not convected along streamlines. Many examples have been computed which have either no embedded shocks or very weak ones, but which have total pressure losses of 30% or more. It is clear that some mechanism other than shock waves is involved.

A possible explanation could be that the losses represent numerical error introduced by the discretization process or added damping terms as represented by Equation (12). In fact this seems to be true, but the interpretation is a bit surprising. Careful numerical studies have been done [13,21] in which grid density and artificial viscosity constants ν_2 and ν_4 were varied by an order of magnitude. The total pressure loss is extremely insensitive to these parameters. See, for example, the table in the previous section. The total pressure loss was also found to be insensitive to grid distribution, initial conditions, and convergence tolerance.

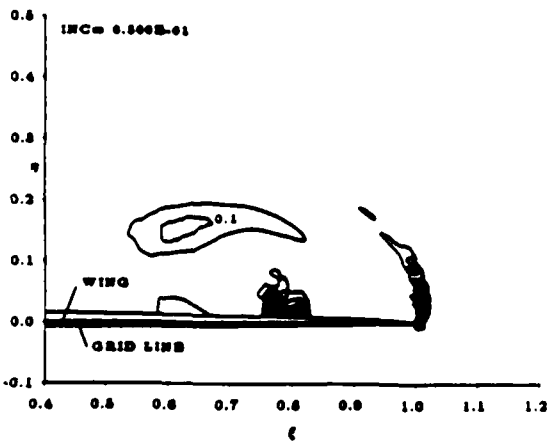

Figure 13: Second order damping magnitude

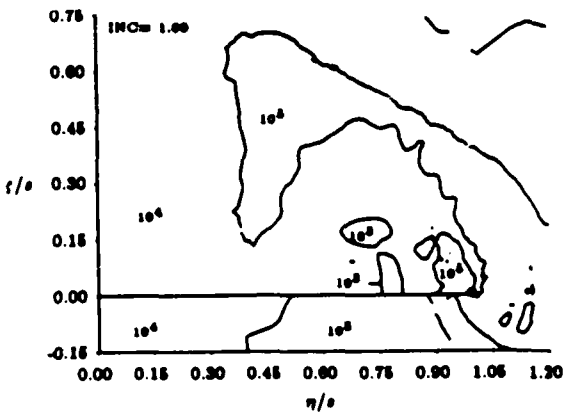

Figure 14: Equivalent Reynolds number

A clue to the source of the losses can be found by comparing the magnitude of the second order damping terms with the sink term H in Equation 12 as shown in Figure 13 taken from [18]. The results are for a $\Lambda = 75°$ flat plate delta wing at $M_\infty = 1.3, \alpha = 10°$ with a 128×128 cell grid. It can be seen that in the feeding sheet region, the vortex core, and around an embedded shock under the vortex, the damping terms are significant.

Further insight can be obtained by looking at a simplified equation set corresponding to the one-dimensional continuity and momentum equations [13]

$$\frac{\partial}{\partial x}(\rho u) = \tilde{\epsilon}_\rho \frac{\partial^2}{\partial x^2}\rho \tag{14}$$

$$\frac{\partial}{\partial x}\left(\rho u^2 + p\right) = \tilde{\epsilon}_{\rho u} \frac{\partial^2}{\partial x^2}(\rho u) \tag{15}$$

where the numerical diffusion coefficients have been denoted by $\tilde{\epsilon}$. Differentiating momentum and using continuity yields

$$\rho u \frac{\partial u}{\partial x} + \frac{\partial p}{\partial x} = \rho \tilde{\epsilon}_{\rho u} \frac{\partial^2 u}{\partial x^2} + u \left(\tilde{\epsilon}_{\rho u} - \tilde{\epsilon}_{\rho} \right) \frac{\partial^2 \rho}{\partial x^2} + 2 \tilde{\epsilon}_{\rho u} \frac{\partial \rho}{\partial x} \frac{\partial u}{\partial x}. \tag{16}$$

Now, if $\tilde{\epsilon}_{\rho u} = \tilde{\epsilon}_{\rho}$, i.e. the same artificial viscosity formulation is used for both continuity and momentum equations which is the usual procedure, then there are only two added terms. The first is a diffusion term, while the last one is a convective term modifying the coefficient of $\frac{\partial u}{\partial x}$. Powell [13] used this idea to define an effective numerical Reynolds number $\sim \tilde{\epsilon}_{\rho u}^{-1}$ which varies throughout the flow field due to mesh resolution, the magnitude of the pressure switch, and the value of $\tilde{\lambda}$. Figure 14 taken from [13] shows the magnitude of the numerical Reynolds number for the same wing as Figure 13 but at $M_\infty = 1.1, \alpha = 10°$. An embedded grid was used such that in the region of interest the grid density is 256×256. Even for such a fine grid, it can be seen that the effective Reynolds number in the primary vortex core is about 10^3!

It is worth keeping in mind that most Navier-Stokes algorithms contain artificial diffusion effects (whether added explicitly as herein or included implicitly as with upwind methods) which are needed for the Euler part of the algorithm. Unless the grid is extremely fine in the vortex region, the artificial diffusion terms probably dominate the real viscous terms in such calculations.

Another interesting numerical result can be understood from Equation 16. A calculation was done in which the second order damping was suppressed from the continuity equation ($\tilde{\epsilon}_{\rho} = 0$) but retained in all the other equations. This had a strong influence on the maximum total pressure loss. It can be seen from (16) that the coefficient $\tilde{\epsilon}_{\rho u} - \tilde{\epsilon}_{\rho}$ does not zero out and an added diffusion term results. By explicitly correcting for this, the calculations with suppressed second differencing damping in the continuity equation gave the same total pressure loss as the original computations. So the magnitude of the total pressure loss is sensitive to the form of the added viscosity, but not to its magnitude. Comparisons between the present finite volume algorithm and results from other algorithms have not shown significant differences, except for the results of Marconi [22] discussed in the last paragraph of this section.

Computational results indicate that the maximum total pressure loss is directly related to the aerodynamic parameters. Variations of Mach number, angles of attack, sweep, and yaw, as well as body geometry all affect the total computed pressure loss in a consistent way. That is, increasing the angle of attack produces stronger vortices and greater total pressure loss as is illustrated in the next section.

The above evidence can be summarized as follows. In the primary vortex core and the shear layer emanating from the wing tip, the added artificial viscosity terms are significant and produce a total pressure loss in a manner similar to what the actual fluid viscosity would produce. The intriguing question is why the total pressure loss is insensitive to the magnitude of the numerical diffusion coefficient. There are different explanations for the core and shear layers. For the core region, the circumferential velocity is brought to zero (see Figure 7) producing a loss. Powell's [13,23] analytical model for a high Reynolds number conical incompressible viscous vortex shows that the only parameter which sets the maximum total pressure loss is the swirl velocity at the edge of the core. As can be seen from the table in the previous section, this parameter is also independent of mesh spacing for the supersonic conical flows. For the shear layer [21], the added viscous terms together with the discrete nature of the solution produce a vortex "sheet" with a thickness related to the mesh spacing. The velocity magnitude should be the same on either side of the sheet, but the direction changes as dictated by the strength of the sheet. Traversing across the sheet, the velocity magnitude will have a minimum in the center leading to a total pressure loss. The reader is referred to [13,23,21,24] for the detailed discussion of these arguments.

The question remains as to whether the artificially introduced total pressure loss is related to the real total pressure loss. Comparisons with measured pitot pressure as given in the previous section and total pressure as given in the next section indicate that although the numerical losses may not be exact, they are a good approximation for compressible flows. For incompressible flows, the agreement is not as good [25], but the studies are not as thorough. The artificial diffusion terms are similar to, but different than, the real diffusion terms even for laminar flows. For Reynolds numbers characteristic of aeronautical applications, the vortex cores will be turbulent. A more physically based numerical viscosity model would be helpful in establishing the accuracy of the predicted total pressure losses.

The final remark of this section addresses the issue of isentropic vortex cores. Marconi [22] has suggested that the correct solution of the Euler equations should only have shock induced total pressure losses. He has used the λ-scheme which integrates the equations in a charactersitic form. Entropy production must be introduced explicitly which only occurs at shock waves. Vortical flows have been computed with zero total pressure losses. By Crocco's equation (13) this means the vorticity and velocity vectors are aligned. The results of these calculations show that the vortex position, surface pressures, and other global features of the flow are in close agreement with solutions which have total pressure losses [22]. Powell [13] modified the present solution algorithm by overriding the streamwise momentum equation with the constant total pressure requirement. Although the iterative convergence rate is poorer, solutions can be obtained and compared with the "lossy" ones. In agreement with Marconi, the global features are the same, but the values of parameters in the vortex cores are different. In particular, the streamwise velocity and Mach number are greater. Comparison with the pitot pressure measurements of Monnerie and Werlé [16] shows much poorer agreement. The present authors feel that the desirable solution of the Euler equations is that which models a viscous flow in the limit of $Re \rightarrow \infty$. The solutions with total pressure losses due to artificial viscosity are more realistic than those with no total pressure loss. Either one seems to be acceptable for prediction of surface pressures and hence forces. However, the two approaches may give different results regarding the prediction of vortex bursting in three-dimensional calculations as total pressure losses can play a role in this phenomenon [26].

Three-Dimensional Solutions

Although the conical Euler model is suitable for studying some of the basic features of leading edge vortex flows, a fully three-dimensional model is needed for realistic wing geometries as well as for subsonic freestream Mach number conditions. In this section, some results using two different grid topologies are presented and compared to experimental data for $M_\infty = .85$. The grids are rather coarse and, therefore, the results should be considered as exploratory. The calculations are for the $\Lambda = 65°$ sharp edge cropped delta wing geometry discussed by Elsenaar and Bütefisch [7]. Much more refined grid solutions for this wing are presented by Wagner and Hitzel [27] and Kumar and Das [28].

The first set of calculations were done by Malecki [29] using an O-O grid supplied by Rizzi and his co-workers (e.g. [8]). A total of 37,768 computational cells were in the field with 2048 cells adjacent to the wing surface. Although 1/16 of the total cells are on the wing, there are only 16 cells between wing and far field. From the conical Euler studies, this is not adequate to give good resolution of the vortex. Also the O-O grid has significant skewness near the cropped tip. Convergence difficulties from this were solved by raising ν_2 to .075 in this area. Only 10° angle of attack was reported by Malecki.

The second set of calculations were done by Goodsell [25] who modified Roberts' program to handle an O-H grid. In planes perpendicular to the flow, an O grid is generated similar to

that used for the conical Euler calculations. A total of 73,728 cells with 768 on the wing surface were used. There are only 12 chordwise stations on the wing, but there are 48 cells between the wing and the far field. Since the vortical flow does not vary rapidly in the streamwise direction, this grid provides better resolution of the crossflow effects than the O-O grid. However, the streamwise transonic effects such as shocks will be poorly resolved. The O-H grid has less skewness than the O-O grid, and has a topology which is more flexible for complicated geometries. Goodsell reported results for $\alpha = 10°, 20°, 24°$, and the former two are discussed here.

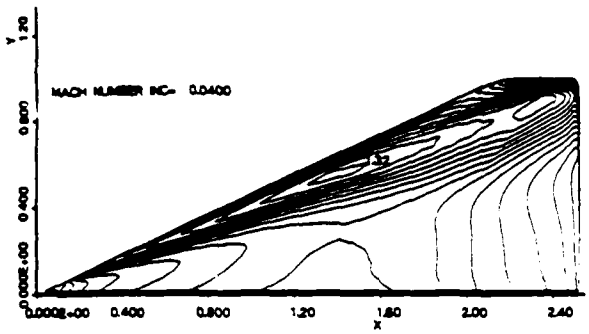

Figure 15: Surface Mach Number, O-O grid. $\alpha = 10°, M_\infty = .85$.

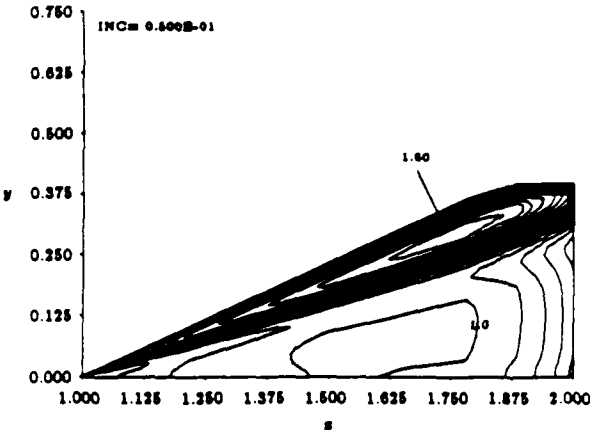

Figure 16: Surface Mach Number, O-H grid. $\alpha = 10°, M_\infty = .85$.

The results for $\alpha = 10°$ correspond to $M_n = .38, \alpha_n = 22.6°$ placing them well within the left hand middle region of Figure 2. Leeside surface Mach number contours for the two topologies are shown in Figures 15 and 16. The footprint of the vortex is evident, and the flow underneath it is supersonic. The O-O grid gives a maximum surface Mach number of 1.32 while the O-H grid with better resolution off the wing surface reaches 1.60. The flow is just supersonic over the mid portion of the wing demonstrating slight streamwise transonic effects for this lowest angle of attack. Finally, both solutions show a shock wave at the tapered tip which is aligned with the streamwise direction. The supersonic outboard flow under the vortex passes through this shock to turn downstream.

Figures 17-19 compare the computed surface pressure coefficients for the O-H grid (lines) with the measurements (symbols) at 30%, 60%, and 80% chord locations. The windward side agreement is good except at 30% chord where the centerbody may have an effect. On the leeward side, it is seen that the calculations predict significantly more suction and that the vortex is located further outboard compared to the experiments. In general the agreement is not too good. Figure 20 shows similar results for the O-O grid at 80% chord location. These calculations show less of a suction peak than the O-H grid results and in general have poorer resolution. The O-O grid calculations have been compared with Rizzi's code using exactly the same grid and are in good agreement [29].

Total pressure loss contours for the O-H grid calculations at 78% chord are shown in Figure 21. Experimental [30] total pressure contours at the 60% chord location are shown in Figure 22 for a wing with the same planform but flat upper surface. The computed results show a loss of 38% while the measurements indicate a loss of 30-40% which is in qualitative agreement. Malecki's calculations with the O-O grid predicted 44% losses at about the 90% chord location.

The results for $\alpha = 20°$ correspond to $M_n = .45, \alpha_n = 40.7°$, again in the left hand middle region of Figure 2. All results are from the O-H grid study [25], and a value of $\nu_2 = .1$ was

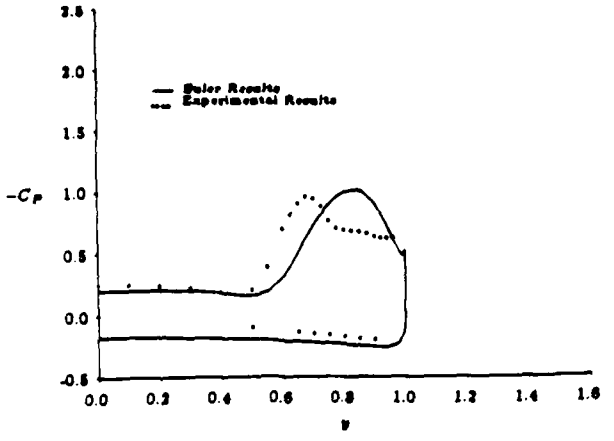

Figure 17: Surface C_p at 30% chord, O-H grid. $\alpha = 10°, M_\infty = .85$.

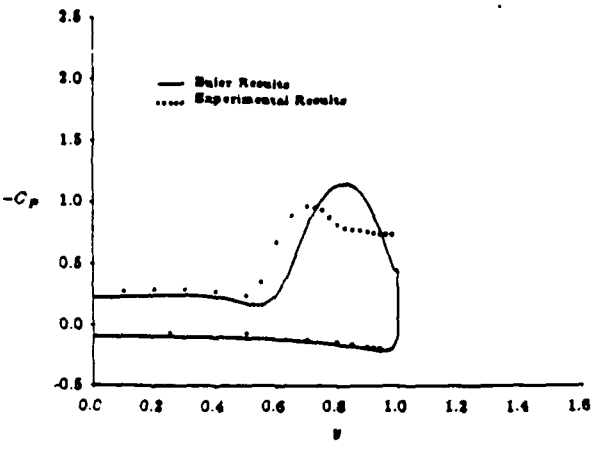

Figure 18: Surface C_p at 60% chord, O-H grid. $\alpha = 10°, M_\infty = .85$.

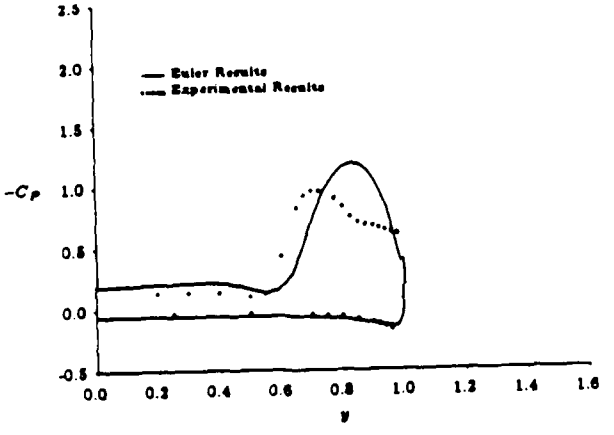

Figure 19: Surface C_p at 80% chord, O-H grid. $\alpha = 10°, M_\infty = .85$.

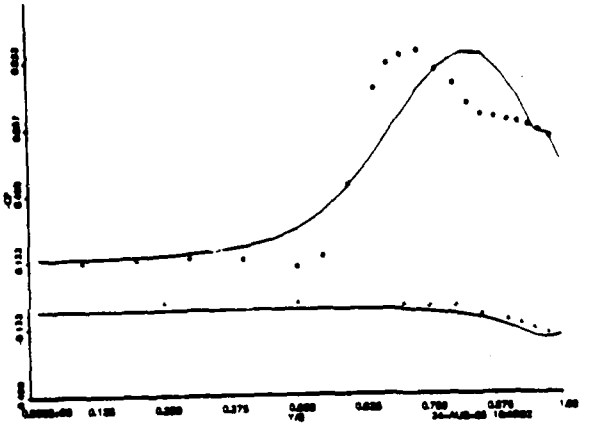

Figure 20: Surface C_p at 80% chord, O-O grid. $\alpha = 10°, M_\infty = .85$.

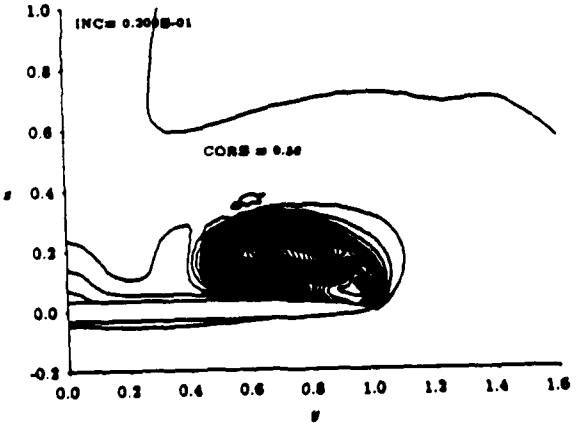

Figure 21: $(1 - P_t/P_{t\infty})$ at 78% chord, O-H grid. $\alpha = 10°, M_\infty = .85$.

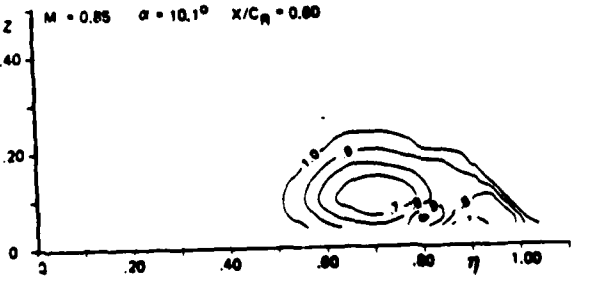

Figure 22: $(P_t/P_{t\infty})$ at 60% chord, measured. $\alpha = 10.1°, M_\infty = .85$.

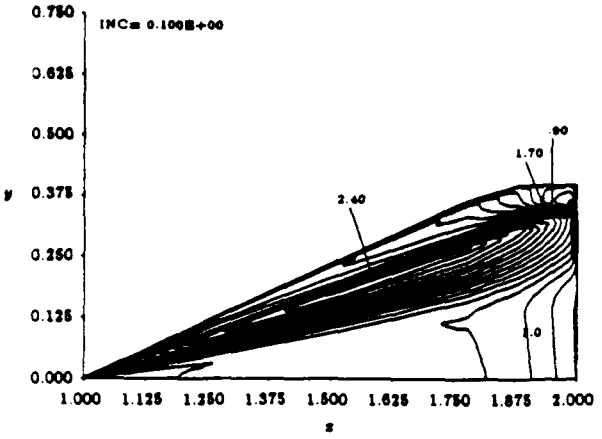

Figure 23: Surface Mach number, O-H grid. $\alpha = 20°, M_\infty = .85$.

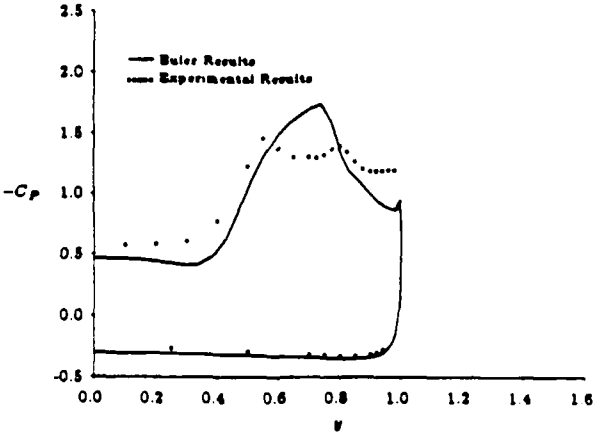

Figure 24: Surface C_p at 60% chord, O-H grid. $\alpha = 20°, M_\infty = .85$.

needed for convergence. The surface Mach number contours of Figure 23 show that the flow is highly transonic. A Mach number of 2.4 is reached under the vortex, and the streamwise flow in the center of the wing is mostly supersonic. The more refined calculations of Wagner and Hitzel [27] show that this supersonic region is terminated by a cross flow shock which interacts with the vortex. The present grid is too coarse to resolve this. The clustering of the contours indicates that there is a shock wave under the vortex. The surface C_p results at the 60% chord, Figure 24 location likewise indicate a strong suction peak terminated by a shock wave. The agreement with the measured C_p data is poor on the leeside due to the viscous effects. The secondary vortex and shock wave-boundary layer interactions significantly reduce the suction peak. A Navier-Stokes model is needed for accurate surface pressure predicitions in this speed regime. The computed and measured total pressure contours are shown in Figures 25 and 26 respectively. Again, there is reasonable agreement between the computed loss of 56% and the measured value of $\simeq 60\%$.

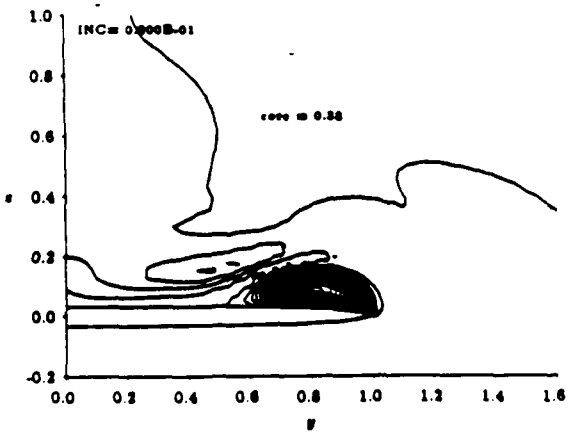

Figure 25: $(1 - P_t/P_{t\infty})$ at 78% chord, O-H grid. $\alpha = 20°, M_\infty = .85$.

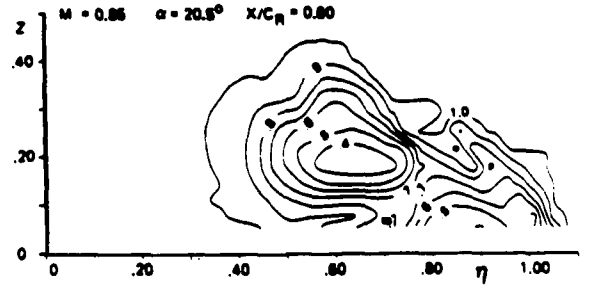

Figure 26: $(P_t/P_{t\infty})$ at 60% chord, measured. $\alpha = 20.5°, M_\infty = .85$.

Conclusions

Leading edge vortices introduce transonic crossflow effects due to their accompanying high swirl velocities. Based upon both calculations and experiments, embedded transonic zones and shock waves are the norm rather than the exception. These effects are in addition to the classical transonic flow features of lifting wings. Numerical solutions of the Euler equations for sharp edge wings appear to model the main effects of the primary vortex. Both analytical and numerical evidence point to the artificial viscosity terms as the source of vorticity. The numerical damping models routinely used by most algorithms seem to lead to realistic total pressure losses. More physically based artificial viscosity models would be desirable. Total pressure deficits may be important in the prediction of vortex bursting. For transonic freestream Mach numbers, the influences of secondary vortex formation and shock wave-boundary layer interaction are important and outside the capabilities of an Euler equation model. For supersonic freestream conditions, the secondary vortex effects have less influence on the leeside pressure distribution.

Acknowledgements

This research was supported by Office of Naval Research Grant N00014-86-K-0288 monitored by Dr. Spyridon Lekoudis.

References

[1] A. Stanbrook and L. C. Squire. Possible Types of Flow at Swept Leading Edges. *Aeronautical Quarterly*, 15(1):72–82, February 1964.

[2] D. S. Miller and R. M. Wood. Leeside Flows over Delta Wings at Supersonic Speeds. *Journal of Aircraft*, 21(9):680–686, September 1984.

[3] D. S. Miller and R. M. Wood. *Lee-Side Flow Over Delta Wings at Supersonic Speeds.* NASA TP 2430, June 1985.

[4] G. Vorropoulos and J. F. Wendt. Laser Velocimetry Study of Compressibility Effects on the Flow Field of a Delta Wing. In *AGARD-CP-342*, April 1983. Paper 9.

[5] J. Szodruch and D. Peake. *Leeward Flow over Delta Wings at Supersonic Speeds.* NASA TM 81187, 1981.

[6] K.Y. Narayan and S.N. Seshadri. Vortical Flows on the Lee-Surface of Delta-Wings. In *Symposium Transsonicum III*, May 1988.

[7] A. Elsenaar and K.A. Bütefisch. Experimental Study of Vortex and Shock Wave Development on the 65-Delta Wing. In *Symposium Transsonicum III*, May 1988.

[8] A. Rizzi, G. Drougge, and B. Müller. Navier Stokes and Euler Solutions for the Vortex Flow Delta Wing. In *Symposium Transsonicum III*, May 1988.

[9] S.S. Desai, R. Rangarajan, U.N. Sinha, and K.S. Ravichandran. On the Development and Application of Software based on the Framework of Cartesian Coordinates. In *Symposium Transsonicum III*, May 1988.

[10] A. Jameson, W. Schmidt, and E. Turkel. *Numerical Solutions of the Euler Equations by a Finite Volume Method Using Runge-Kutta Time-Stepping Schemes.* AIAA-81-1259, June 1981.

[11] T.W. Roberts. *Euler Equation Computation for the Flow Over a Hovering Helicopter Rotor.* PhD thesis, Massachusetts Institute of Technology, November 1986.

[12] A. Rizzi and L. E. Eriksson. Computation of Flow around Wings Based on the Euler Equations. *Journal of Fluid Mechanics*, 148, November 1984.

[13] K.G. Powell. *Vortical Solutions of the Conical Euler Equations.* PhD thesis, Massachusetts Institute of Technology, June 1987. To be published by Vieweg as a Volume of Notes On Numerical Fluid Mechanics.

[14] E. Murman, A. Rizzi, and K. Powell. High Resolution Solutions of the Euler Equations for Vortex Flows. In *Progress and Supercomputing in Computational Fluid Dynamics*, pages 93–113, Birkhauser-Boston, 1985.

[15] S.N. McMIllin, J.L. Thomas, and E.M. Murman. *Euler and Navier-Stokes Solutions for the Leeside Flow Over Delta Wings at Supersonic Speeds.* AIAA-87-2270, August 1987.

[16] B. Monnerie and H. Werlé. Étude de l'Écoulement Supersonique & Hypersoniqui autour d'une Aile Élancée en Incidence. In *AGARD-CP-30*, 1968. Paper 23.

[17] E.M. Murman and K.G. Powell. Trajectory Integration in Vortical Flows. Technical note to appear in AIAA J.

[18] E.M. Murman, K.G. Powell, A. M. Goodsell, and M. Landahl. *Leading Edge Vortex Solutions With Large Total Pressure Losses.* AIAA-87-0039, January 1987.

[19] *Equations, Tables, and Charts for Compressible Flow.* NACA TR 1135.

[20] R. W. Ladenburg, B. Lewis, R. N. Pease, and H. S. Taylor, editors. *Physical Measurements in Gas Dynamics and Combustion.* Princeton University Press, 1964.

[21] K. Powell, E. Murman, E. Perez, and J. Baron. *Total Pressure Loss in Vortical Solutions of the Conical Euler Equations.* AIAA-85-1701, July 1985.

[22] F. Marconi. *Flat Plate Delta Wing Separated Flows with Zero Total Pressure Losses.* AIAA-87-0038, January 1987.

[23] K.G. Powell and E.M. Murman. *A Model for the Core of a Slender Viscous Vortex.* AIAA-88-0503, January 1988.

[24] K.G. Powell and E.M. Murman. An Embedded Mesh Procedure for Leading-Edge Vortex Flows. In *Proceedings of NASA Langley Transonic Symposium*, Springer-Verlag, 1988.

[25] Goodsell A.M. *3-D Euler Calculations of Vortex Flows Over Delta Wings.* Master's thesis, Massachusetts Institute of Technology, July 1987.

[26] M. G. Hall. Vortex Breakdown. In *Annual Review of Fluid Mechanics - Vol 4*, pages 195–217, Annual Reviews, Inc., 1972.

[27] B. Wagner and S.M. Hitzel. Computations Relating to the Vortex Flow Experiment. In *Symposium Transsonicum III*, May 1988.

[28] A. Kumar and A. Das. Computations of Vortex Flow on a Delta Wing at Transonic Speed. In *Symposium Transsonicum III*, May 1988.

[29] R.E. Malecki. *Euler Equation Calculations for a Cropped Delta Wing Using the CYBER 205.* Master's thesis, Massachusetts Institute of Technology, August 1986.

[30] A. Elsenaar, L. Hjelmberg, K.A. Bütefisch, and Bannink W.J. The International Vortex Flow Experiment. In *Lisbon Conference*, AGARD, May 1988.